



## Article

# Lead-Free Perovskite Thin Films for Gas Sensing through Surface Acoustic Wave Device Detection

Nicoleta Enea<sup>1,2,3</sup> , Valentin Ion<sup>1,\*</sup> , Cristian Viespe<sup>1</sup> , Izabela Constantinoiu<sup>1</sup> , Anca Bonciu<sup>1</sup> , Maria Luiza Stîngescu<sup>1,3</sup> , Ruxandra Birjega<sup>1</sup> and Nicu Doinel Scarisoreanu<sup>1</sup>

<sup>1</sup> National Institute for Laser, Plasma and Radiation Physics, 077125 Magurele, Romania; nicoleta.enea@inflpr.ro or nicoleta.enea@unifi.it (N.E.); cristian.viespe@inflpr.ro (C.V.); izabela.constantinoiu@inflpr.ro (I.C.); anca.bonciu@inflpr.ro (A.B.); maria.stingescu@inflpr.ro (M.L.S.); ruxandra.birjega@inflpr.ro (R.B.); nicu.scarisoreanu@inflpr.ro (N.D.S.)

<sup>2</sup> Department of Physics and Astronomy, University of Florence, Via G. Sansone 1, 50019 Sesto Fiorentino, FI, Italy

<sup>3</sup> Faculty of Physics, University of Bucharest, 077125 Magurele, Romania

\* Correspondence: valentin.ion@inflpr.ro; Tel.: +40-21-457-4550

**Abstract:** Thin film technology shows great promise in fabricating electronic devices such as gas sensors. Here, we report the fabrication of surface acoustic wave (SAW) sensors based on thin films of  $(1-x)\text{Ba}(\text{Ti}_{0.8}\text{Zr}_{0.2})\text{O}_{3-x}(\text{Ba}_{0.7}\text{Ca}_{0.3})\text{TiO}_3$  (BCTZ50,  $x = 50$ ) and Polyethylenimine (PEI). The layers were deposited by two laser-based techniques, namely pulsed laser deposition (PLD) for the lead-free material and matrix assisted pulsed laser evaporation (MAPLE) for the sensitive polymer. In order to assay the impact of the thickness, the number of laser pulses was varied, leading to thicknesses between 50 and 350 nm. The influence of BCTZ film's crystallographic features on the characteristics and performance of the SAW device was studied by employing substrates with different crystal structures, more precisely cubic Strontium Titanate ( $\text{SrTiO}_3$ ) and orthorhombic Gadolinium Scandium Oxide ( $\text{GdScO}_3$ ). The SAW sensors were further integrated into a testing system to evaluate the response of the BCTZ thin films with PEI, and then subjected to tests for  $\text{N}_2$ ,  $\text{CO}_2$  and  $\text{O}_2$  gases. The influence of the MAPLE's deposited PEI layer on the overall performance was demonstrated. For the SAW sensors based on BCTZ/ $\text{GdScO}_3$  thin films with a PEI polymer, a maximum frequency shift of 39.5 kHz has been obtained for  $\text{CO}_2$ ; eight times higher compared to the sensor without the polymeric layer.

**Keywords:** thin film; PLD; MAPLE; BCTZ; lead-free piezoceramic; PEI,  $\text{CO}_2$  and  $\text{O}_2$  detection; SAW sensor



**Citation:** Enea, N.; Ion, V.; Viespe, C.; Constantinoiu, I.; Bonciu, A.; Stîngescu, M.L.; Birjega, R.; Scarisoreanu, N.D. Lead-Free Perovskite Thin Films for Gas Sensing through Surface Acoustic Wave Device Detection. *Nanomaterials* **2024**, *14*, 39. <https://doi.org/10.3390/nano14010039>

Academic Editor: Sergei A. Kulnich

Received: 29 November 2023

Revised: 18 December 2023

Accepted: 20 December 2023

Published: 22 December 2023



**Copyright:** © 2023 by the authors. Licensee MDPI, Basel, Switzerland. This article is an open access article distributed under the terms and conditions of the Creative Commons Attribution (CC BY) license (<https://creativecommons.org/licenses/by/4.0/>).

## 1. Introduction

In an era where the demand for air quality monitoring to ensure the safety of the environment and human health has increased, gas sensors have become crucial for the detection of various gases (such as volatile organic compounds [1], inorganic gases [2–10], etc.). In the last few decades, surface acoustic wave (SAW) technology has been integrated into gas detection devices, providing them with attractive advantages such as compactness, portability, low-cost manufacturing, high sensitivity and accuracy, real-time measurements and good reliability [11–13]. Moreover, through a suitable choice of materials for fabricating these types of sensors, they also offer outstanding characteristics like selectivity, reversibility and linearity [14]. An SAW gas sensor (Rayleigh-wave, delay-line type sensor) consists of an expensive piezoelectric single-crystal material (usually ST-Quartz or  $\text{LiNbO}_3$ ) with interdigital transducer electrodes (IDTs) deposited on its surface and a recognition layer in-between.

SAW devices convert the input electrical signal sent through IDT into a mechanical one, which is subsequently altered by the sensing event and converted back into an electrical one through the output IDT. The changes produced by the exposure of the detection layer

to the target analyte consist of variations in the amplitude, frequency and phase of the output signal relative to the input signal [15–17].

Regarding the sensing layers, a wide range of materials have been exploited for these SAW devices [11,18,19]. Common materials such as conductive/non-conductive polymers and metal oxides have been chosen most often to recognise gas molecules [20,21]. But other materials have also been tested, including carbon-based nanostructures [22–25], composite materials [26,27], metals [28], metal-organic frameworks [29] and porous materials [30]. There are some reports in the literature on using a ferroelectric lead zirconium titanate (PZT) thin film as the sensing layer to improve the coupling coefficient of SAW devices [3,31,32]. In addition, a low-cost SAW device based on a thin layer of PZT deposited on a non-piezoelectric substrate was reported [33], but detailed studies on the use of thin films of lead-free ferroelectric materials for gas sensing in SAW devices are scarce. Multi-component systems of lead titanate ( $\text{PbTiO}_3$ ) and lead zirconate ( $\text{PbZrO}_3$ ), called lead zirconium titanate ( $\text{Pb}[\text{Zr}_x\text{Ti}_{1-x}]\text{O}_3$  ( $0 \leq x \leq 1$ )—PZT), are the most widely employed perovskite ceramic materials due to their advantageous properties, such as greater sensitivity and higher operating temperature, compared to other piezo ceramics [34,35]. Since 2006, legislation restricts the use of materials that pose risks to human health and to the environment, thus lead-based materials are considered to be particularly toxic and, in this regard, the attention of researchers has turned to other lead-free piezoelectric materials.

Among this class of eco-friendly materials, barium titanate ( $\text{BaTiO}_3$ -BT) was the first ceramic material with ferroelectric properties ever discovered, but the interest in it declined after the discovery of PZT, whose piezoelectric properties were superior [36]. The potential of using BT-based ceramics in piezoelectric applications was reconsidered after 2009, when Liu and Ren found a surprisingly high piezoelectric coefficient ( $d_{33} \sim 620$  pC/N) for the non-lead ceramic system  $\text{Ba}(\text{Ti}_{0.8}\text{Zr}_{0.2})\text{O}_3 - (\text{Ba}_{0.7}\text{Ca}_{0.3})\text{TiO}_3$  [37]. This strategy for improving the piezoelectric response of BT by introducing  $\text{Ca}^{2+}$  and  $\text{Zr}^{4+}$  into its crystal structure has led to increased research papers on this topic [38]. Lead-free piezoelectric materials  $(\text{Ba}, \text{Ca})(\text{Ti}, \text{Zr})\text{O}_3$  (BCTZ) with different properties were obtained by varying the concentrations of the two ferroelectric oxides  $\text{Ba}(\text{Ti}_{0.8}\text{Zr}_{0.2})\text{O}_3$  and  $(\text{Ba}_{0.7}\text{Ca}_{0.3})\text{TiO}_3$ , which enables their use in applications such as energy harvesting and storage or actuators. Different techniques for growing thin layers of BCTZ on various substrates have been reported in the literature, from chemical ones, like the sol-gel method [39], to physical ones, namely, RF magnetron sputtering [40] and pulsed laser deposition [41].

Using polymer-inorganic composites was demonstrated to result in high-performance gas sensors due to the synergistic effects [42] between specific functional materials when used with an adequate fabrication technology. Numerous polymers can be used as sensing materials, for instance, polypyrrole (PPy), polyaniline (Pani) or polythiophene and their derivatives [43,44]. In this present work, we selected polyethylenimine (PEI) to obtain hybrid layers of polymer-inorganic composites.

Motivated by the possibility of using lead-free piezoelectric/ferroelectric materials for SAW devices [3], [33], here we report the fabrication and functional properties of surface acoustic wave (SAW) sensors based on thin films of  $(1 - x) \text{Ba}(\text{Ti}_{0.8}\text{Zr}_{0.2})\text{O}_3 - x(\text{Ba}_{0.7}\text{Ca}_{0.3})\text{TiO}_3$  (BCTZ50) in combination with a Polyethylenimine (PEI) layer, using laser-based deposition techniques to obtain both inorganic and organic layers. As the various characteristics of an active sensor element (i.e., thickness, crystalline structure, surface roughness, chemistry, etc) can influence the response of an SAW sensor to a specific analyte, the thin layers of BCTZ50 were deposited by pulsed laser deposition (PLD) onto different monocrystalline substrates ( $\text{SrTiO}_3$ ,  $\text{GdScO}_3$ ) to induce different epitaxial characteristics (strain, texture) into the film's crystalline structure. This was followed by depositing a PEI polymer on top of the epitaxial BCTZ50 thin films using the matrix assisted pulsed laser evaporation (MAPLE) technique. The structures obtained were further integrated into SAW devices to evaluate their sensing properties in different gaseous environment.

## 2. Materials and Methods

### 2.1. Deposition of Thin Films

The  $(1 - x) \text{Ba}(\text{Ti}_{0.8}\text{Zr}_{0.2})\text{O}_{3-x}(\text{Ba}_{0.7}\text{Ca}_{0.3})\text{TiO}_3$  (BCTZ $x$ ) thin films were deposited by pulsed laser deposition (PLD) using the  $x = 50$  composition.

BCTZ50 targets were prepared via the conventional sintering route, starting from precursors and followed by milling, pressing and sintering at high temperature (1450 °C).

The substrates used for deposition were monocrystalline Strontium Titanate ( $\text{SrTiO}_3$  or STO) and Gadolinium Scandium Oxide ( $\text{GdScO}_3$  or GSO). For the fabrication of the BCTZ50/STO and BCTZ50/GSO samples, an ArF excimer laser was used, the laser fluence value being  $1.65 \text{ J/cm}^2$ . The number of laser pulses ranged between 8000 and 36,000, with a 5 Hz repetition rate. The substrate temperature was set to 700 °C, with a heating rate of 50 °C/min while the cooling rate was set to 10 °C/min. The flow of oxygen during the ablation process was set to 20 sccm and the gas pressure reached  $1 \times 10^{-1}$  mbar, before starting laser ablation. When the ablation process ended, the cooling of the substrates was performed in oxygen flow, set to 200 sccm.

The Polyethylenimine (PEI) polymer was deposited using matrix assisted pulsed laser evaporation (MAPLE). The MAPLE deposition method involves obtaining a target from a polymer dissolved in a solvent (matrix). The PEI target was obtained by dissolving 400 mg of PEI in a 1:1 solution of deionised water and isopropyl alcohol, under magnetic stirring, for 60 min. The target thus obtained was frozen in liquid nitrogen and further irradiated, using 266 nm of a Nd:YAG laser, at 10 Hz with 36,000 laser pulses.

The surface acoustic wave sensors (SAW) were used to evaluate the response of BCTZ thin film covered and uncovered with PEI. For the gas response measurement, interdigital electrodes were deposited on the surface of thin films via thermal evaporation.

For the IDT, Au metal electrodes were deposited, with thicknesses of approximately 200 nm on the BCTZ thin layers. Later, gold wires with a diameter of 75  $\mu\text{m}$  were glued to the electrodes, using an epoxy conductive silver (Ag). The sensors were tested and characterised for different types of usual gases ( $\text{O}_2$ ,  $\text{CO}_2$  and  $\text{N}_2$ ), at room temperature and with a humidity of 60%. The humidity was monitored using a hygrometer.

Using the methods and techniques described above, an evaluation of the gas response of BCTZ50 and PEI/BCTZ50 structure was conducted.

### 2.2. Thin Layer Characterization

In this study, we explored the surface morphology of the samples through scanning electron microscopy (SEM). Our analyses were performed using the Scios 2 DualBeam, an advanced ultra-high-resolution analytically focused ion beam scanning electron microscopy FIB-SEM system (Thermo Fisher Scientific Inc. in Hillsboro, OR, USA), at voltages reaching up to 30 kV. The topography of the probes was further analysed by employing atomic force microscopy (AFM) (XE 100 AFM, Park systems KANC 15F, Gwanggyo-ro, Suwon, Republic of Korea) and the measurements were performed in non-contact mode.

Optical properties were investigated by spectroscopic ellipsometry measurements on a Woollam Variable Angle Spectroscopic Ellipsometer (VASE) system equipped with a high-pressure Xe discharge lamp. The spectral range analysed was 1–5 eV, representing the near IR to the UV (260–1200 nm) spectrum and was carried out at a fixed angle of incidence. For obtaining the refractive indexes and extinction coefficients of the analysed layers, WVASE32 software (VASE, J.A. Woollam Co., Inc., Lincoln, NE, USA) was used for fitting and extracting the data from complex multilayer response.

High-resolution X-ray diffraction was conducted on a PANalytical X'pert MRD system (Almelo, The Netherlands) using a parallel monochromatic beam of  $\text{CuK}\alpha_1$  ( $\lambda = 1.540598 \text{ \AA}$ ) provided by a four-bounce crystal of Ge(220) placed in the incident beam.

### 2.3. SAW Measurements

The SAW testing system was composed of an amplifier (DHPVA-200 FEMTO amplifier—Messtechnik GmbH, Berlin, Germany), a frequency counter (CNT-91 Pendulum—Spectracom

Corp, Rochester, NY, USA) connected to a computer with specialised software. The gas flow was ensured by a mass flow controller, through a mass flow meter, and the gas concentration used for testing was:  $N_2$ —99.996%;  $CO_2$ —99.998%; and  $O_2$ —99.999%; with a gas flow of 0.5 L/min. All investigations were performed at room temperature.

### 3. Results and Discussion

#### 3.1. AFM and SEM Morphological Characterization

Scanning electron microscopy and atomic force microscopy were used first to analyse the morphology and roughness of the deposited coatings surfaces. Examples of the SEM images with a magnification of 20 k of the samples obtained by PLD are presented in Figure 1.

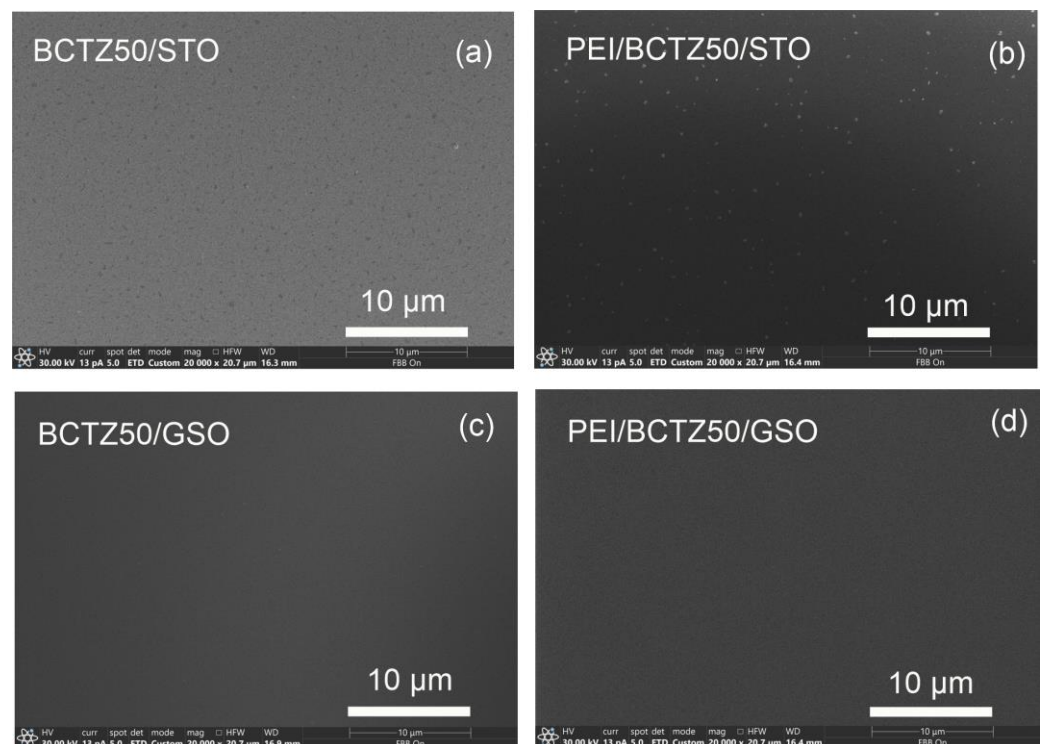


**Figure 1.** SEM images of thin films deposited on (STO) heated at 700 °C in mbar of oxygen (a) BCTZ50/STO; (b) PEI/BCTZ50/STO; (c) BCTZ50/GSO and (d) PEI/BCTZ50/GSO.

The SEM analysis provided valuable insights into the characteristics of thin films deposited using Pulsed Laser Deposition (PLD) on different substrates. Specifically, when applied to Strontium Titanate (STO) substrates, PLD consistently yielded thin films with a uniform distribution across the surface. However, a notable observation was the regular accumulation of material in the form of grains on the surface; a phenomenon commonly associated with PLD technique.

Despite the presence of these surface grains, an interesting finding emerged: the overall appearance and characteristics of the film surfaces did not undergo significant changes even when the number of pulses was varied. This suggests a robustness in the PLD-deposited films on STO substrates, as their fundamental properties appeared to remain stable under different deposition conditions.

In contrast to the STO substrates, the examination of Barium Calcium Titanate Zirconate (BCTZ) films on Gadolinium Scandium Oxide (GSO) revealed a distinctly different outcome. The SEM analysis highlighted the remarkably smooth surface morphology for the BCTZ film on GSO. This indicates that the interaction between the PLD technique and the GSO substrate resulted in a unique deposition behaviour, leading to a more even and homogeneous film surface.

These observations not only contribute to our understanding of the PLD process, but also underscore the significance of substrate selection in determining the final morphology of thin films. The ability to control and manipulate the surface characteristics of deposited films is crucial for various applications.

For a better visualization of the surface topography, and to understand the material organization on the surfaces, AFM measurements were performed.

The influence of the substrate can easily be seen through the appearance of columnar grains of maximum 40 nm, in the case of the thin film deposited on GdScO<sub>3</sub>, compared with the one on SrTiO<sub>3</sub>, where the surface morphology became smoother. In all cases, the surface was uniformly covered by the deposited thin films, with no defects, and the roughness of the layers was found to be between 4 and 40 nm.

In contrast with the BCTZ samples, the main characteristic for the PEI/BCTZ layered coatings, as confirmed by both SEM and AFM analysis, is a low roughness on the surface, as can be seen in Figures 1b and 2c. MAPLE-deposited PEI layers were smooth, with no cracks, and the two employed analysis techniques revealed uniformly distributed films, covering the entire surface of the probes, in accordance with other studies published in the literature [45].

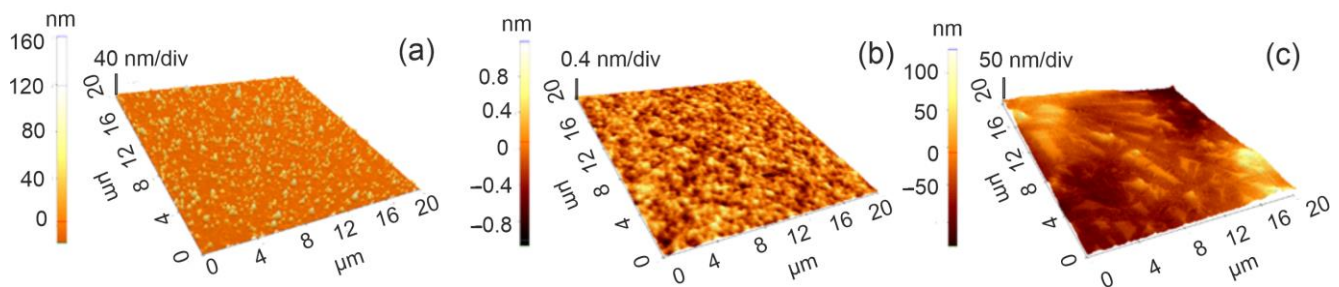


**Figure 2.** AFM topography images for 36,000 laser pulses BCTZ thin films (a) BCTZ50/GSO (b) BCTZ50/STO and (c) PEI/BCTZ50/STO.

### 3.2. XRD Measurements

The films were deposited on (001)-oriented cubic STO substrates and (110)-oriented orthorhombic GSO substrates, respectively. For simplicity, and for comparison, we considered a pseudocubic lattice for GSO. The orthorhombic (110) orientation of GSO is equivalent to the (001) of a pseudocubic symmetry, and consequently, the substrates were prescribed the subscript “pc” for GSO and “c” for STO. STO has a cubic lattice parameter of 3.905 Å, and GSO has a pseudocubic lattice parameter of 3.967 Å [46]. Figure 3 displays the conventional X-ray  $2\theta$ - $\theta$  scans for the BCZT films on (b) STO and (c) GSO substrates. The  $x = 50$  value for BCZT target is, at room temperature, near the morphotropic phase boundary (MPB) separating the rhombohedral (R) and tetragonal (T) phases by an intermediate orthorhombic (O) phase. The target BCZT50 XRD patterns exhibits a distorted orthorhombic phase which we had refined in a cubic symmetry (S.G. Pm-3m) to obtain a pseudocubic lattice parameter of 4.0118 Å [47], consistent with the standard BCZT powder XRD pattern, ICDD card no. 00-063-0614 (Figure 3a). All the films show only the (00 $l$ ) reflections with no secondary phase, revealing a fully epitaxial growth. The epitaxial coherent growth of the BCZT films is confirmed by the four-circle  $\Phi$  scans around (101) BCZT and their corresponding (101)<sub>c</sub> STO and (101)<sub>pc</sub>-GSO reflections, respectively. For all the films, a fourfold symmetry is clearly seen (Figure 4).

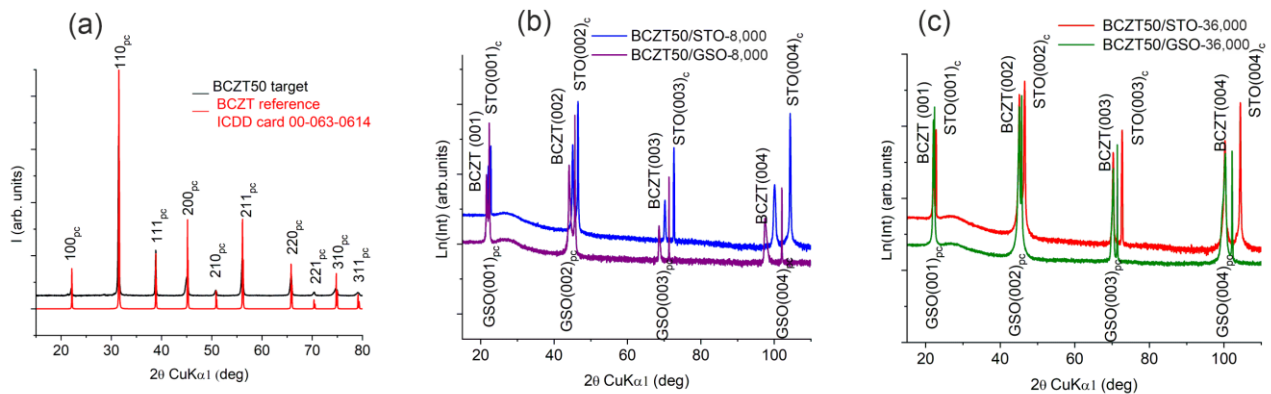


**Figure 3.** XRD patterns of the BCZT. (a) BCTZ standard card ICDID card no. 00-063-0614 and BCTZ50 target; (b) thin films deposited on GSO with 8000 laser pulses; (c) thin films deposited on STO with 36,000 laser pulses.

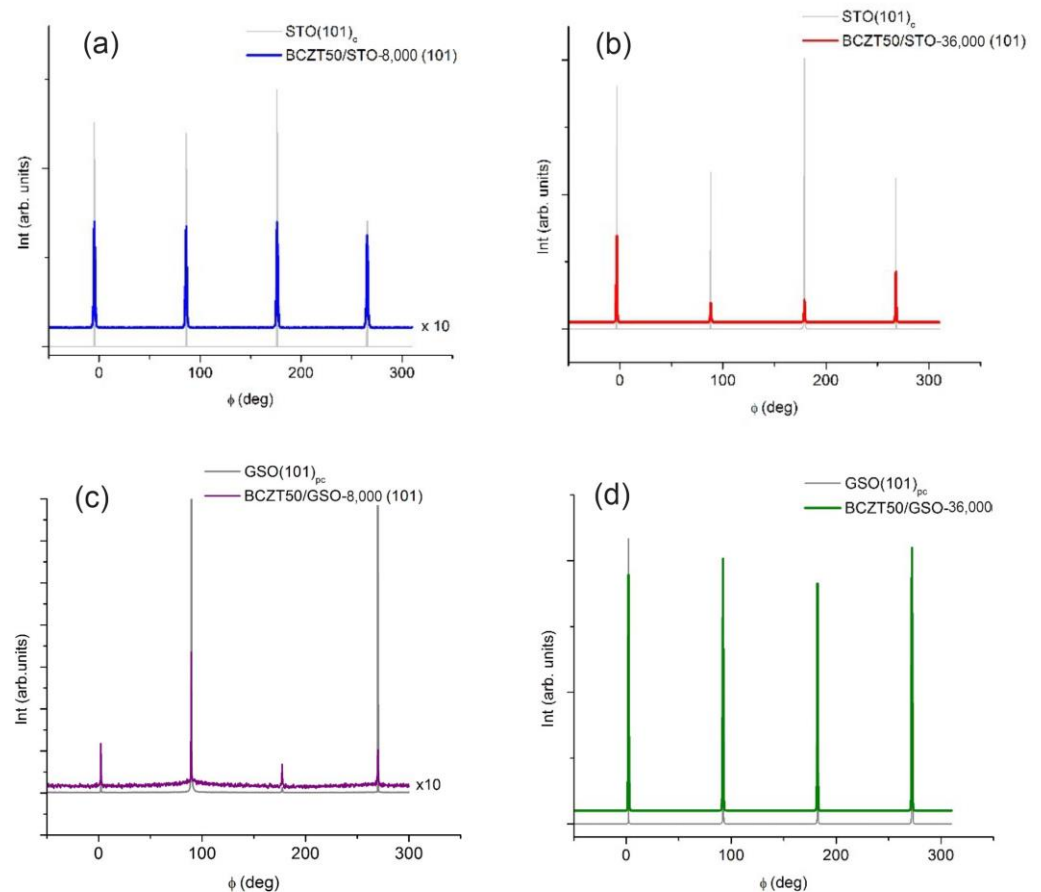


**Figure 4.** XRD four-circle  $\Phi$  scans around (101) BCZT reflection for (a,b) BCTZ/STO films with different thickness and (c,d) BCTZ/GSO films with different thickness.

The out-of-plane and in-plane lattice parameters were determined from conventional and off-axis scans. The mosaicity of the films is described by the  $\omega$ -scans of the (00 $l$ ) symmetric reflections. Figure 5 presents the superimposed  $\omega$ -scans of the (002) reflections of the BCZT50 films deposited on STO and GSO. From the evolution of the broadening of these  $\omega$ -scans of the (00 $l$ ) reflections, using the Williamson–Hall approach proposed by Mentzger et al. [48], the lateral coherence length, which is parallel to the substrate ( $L_{\parallel}$ ), and the mean mosaic tilt angle ( $\alpha_{\text{tilt}}$ ) were extracted. We employed the approach described in our previous works [41,47]. The structural data are gathered in Table 1, along with the

values of the degree of the in-plane strain due to the misfit relative to the substrate,  $\varepsilon_{in-plane}$ , calculated as  $(a_{in-plane} - a_{substrate})/a_{substrate} * 100\%$ .

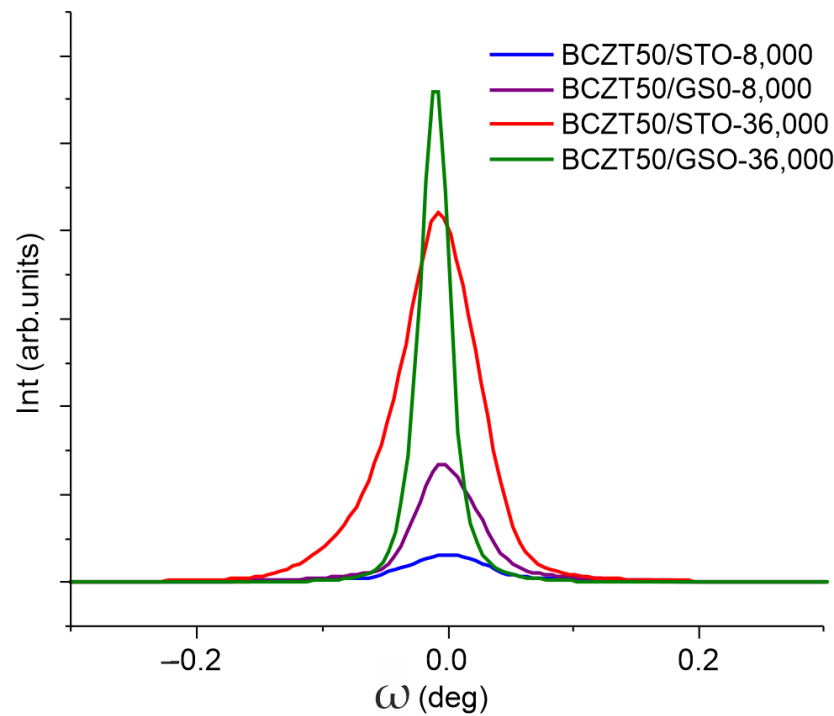


**Figure 5.** XRD X-ray rocking curves ( $\omega$ -scans) of the BCZT (002) reflections for the films deposited on STO and GSO substrates.

**Table 1.** Structural data extracted from XRD analysis.

Probe	Laser Pulses	$a_{out-of-plane}$ (Å)	$a_{in-plane}$ (Å)	In-Plane Strain- $\varepsilon_{in-plane}$ (%)	FWHM- $\omega(002)$ (deg)	$L_{II}$ (nm)	$\alpha_{tilt}$ (deg)
BCZT50/STO	8000	4.0193	4.0173	2.88	0.068	72	0.227
BCZT50/GSO	8000	4.1022	3.9799	0.33	0.056	270	0.096
BCZT50/STO	36,000	4.0152	3.9857	2.07	0.078	376	0.051
BCZT50/GSO	36,000	4.0162	4.0147	1.20	0.031	471	0.054

An examination of the structural data collected in Table 1 shows the results to be related to the nature of the substrate (STO or GSO) and to the thickness of the films controlled by the used number of laser pulses. Furthermore, one can see that the smallest in-plane strain values are obtained for the thin films deposited onto GSO, due to GSO's larger pseudocubic lattice parameter. Apparently, the thickness of the thin films affects their mosaicity: the lateral coherence length increases with the thickness while the mean mosaic tilt angle decreases.

With the improved mosaicity, the crystallinity of the thicker-strained relaxed films is clearly emphasised by the broadness of rocking curves in the BCZT (002) plane, as presented in Figure 5. However, for the thin films deposited onto GSO substrates, one should bear in mind the actual orthorhombic symmetry of the substrate which induces anisotropic strains in the BCZT films, which generates interesting structural features [49].

### 3.3. Optical Properties: Spectrometric Ellipsometry (SE)

Ellipsometry measurements were carried out to evaluate the optical properties of BCTZ samples by performing measurements in the 260–1200 wavelength nm range, at

room temperature. The  $\Delta$  and  $\psi$  parameters are the phase difference and amplitude ratio in the electric field; they describe the change in polarization (from circular to elliptic polarization) and were fitted by building an optical model. The change in polarization state occurs when the incident light beam interacts with measured structure.  $\Delta$  and  $\psi$  depend on the optical properties of the analysed structures and the thicknesses of material layers. In this case, the samples were thin layers of BCTZ deposited on monocrystalline substrates (SrTiO<sub>3</sub> and GdScO<sub>3</sub>). The optical model consisted of a stack of three layers: the substrate, the deposited BCTZ layer and the rough top layer. Each layer was characterised by its own dielectric function (optical properties). For the monocrystalline substrates, we performed the SE measurement before the PLD deposition and we calculated the dispersion of “ $n$ ” and “ $k$ ” by fitting  $\Delta$  and  $\psi$  and using point-by-point regression analysis [50]. The BCTZ layer was fitted by a single Gauss oscillator and the top rough layer was assumed to consist of 50% air and 50% BCTZ in a Bruggeman approximation.

The calculated thicknesses of the BCTZ layer and the value of roughness are presented in Table 2. In the case of BCTZ50 deposited with 8000 laser pulses, thicknesses values between 60 and 100 nm were obtained, with a roughness of a few nanometres. When the number of laser pulses increased to 36,000, the obtained thickness was more than three times higher. There was no linear relation between laser pulses and the calculated thickness, even if the rest of deposition parameters were kept constant (oxygen pressure, distance between target and substrate, laser fluency and substrate temperature) during the PLD process.

**Table 2.** The values of thicknesses and the Gauss parameters for the BCTZ samples growth by PLD.

Probe	Laser Pulses	Thickness (nm)	Roughness (nm)	Amp Gauss	En (eV)	Br (eV)	MSE
BCTZ 50/STO	8000	93.3	2.1	9.31	4.70	1.02	2.777
BCTZ 50/STO	36,000	314.9	1.3	12.29	4.93	1.12	1.374
BCTZ 50/GSO	8000	67.2	2.8	11.39	4.92	1.17	2.803
BCTZ 50/GSO	36,000	340.1	9.1	11.94	4.89	1.08	8.395

When using 36,000 laser pulses, the thickness increased a few times and there were no significant differences between the values of refractive indexes in the visible-IR spectral zone (Figure 6). Nevertheless, the extinction coefficient values were slightly different. For the 8000 BCTZ sample, “ $k$ ” was higher ( $k \sim 0.6$  at  $\lambda = 300$  nm, compared to  $k \sim 0.4$  for 36,000 pulses) and the difference can be explained by the strain induced in the thin film caused by the difference between the SrTiO<sub>3</sub> substrate lattice constant (cubic with  $a = 3.905$  Å) and the lattice constant of BCTZ50 (*pseudo-cubic with  $a(pc) = 4.0118$  Å*). When the sample thickness increased, the thin film relaxed, and the properties were found to be similar with bulk BCTZ. For BCTZ thin film deposited on STO, because there is a difference between the Zr and Ca atom radii, which led to slightly different packing density, we obtained different values of optical constants.

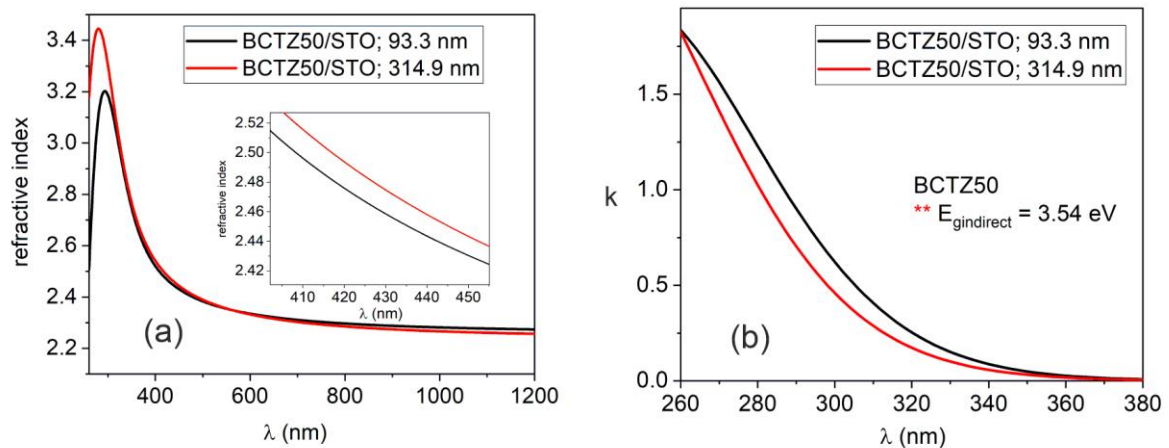


**Figure 6.** Comparison between the dispersion of optical constants for the BCTZ50/STO thin layer growth at 8000 and 36,000 laser pulses: (a) refractive index and (b) extinction coefficients. In caption zoom of refractive index for samples in UV spectral region

In the case of a BCTZ thin layer grown on  $\text{GdScO}_3$  monocrystalline substrate, a similar optical behaviour to the BCTZ $x$  grown on STO was obtained (Figure 7).

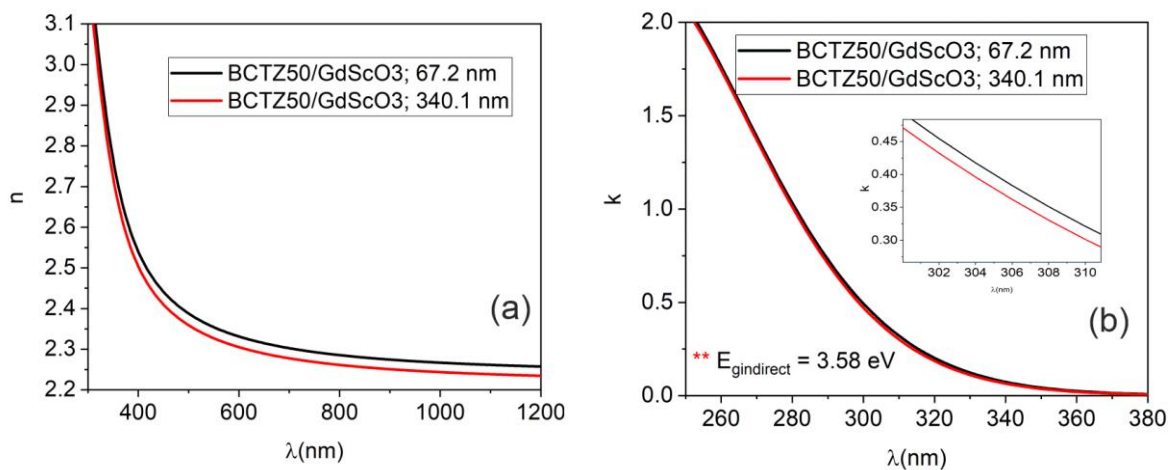


**Figure 7.** The values of optical constants for the BCTZ50 thin layers deposited on  $\text{GdScO}_3$  substrate at (a) 8000 and (b) 36,000 laser pulses: (a) refractive index and (b) extinction coefficients. In caption zoom of extinction coefficients for samples in UV spectral region

For the band gap calculation, Tauc plotting was employed [46]. By plotting the absorption coefficient  $\alpha$  ( $\alpha = 4\pi k/\lambda$ ) as a function of photon energy (eV), the values of the band gap are obtained.  $\text{BaTiO}_3$  (BTO) in a tetragonal structure presents with an indirect band gap [47], with an energy value of 3.41 eV. Instead of BTO, the value of the indirect band gap for BCTZ50 grown on STO substrate was found to be higher,  $E_{g\text{indirect}} = 3.54$  eV.

In the case of a BCTZ thin layer grown on a  $\text{GdScO}_3$  monocrystalline substrate, a similar optical behaviour to the BCTZ $x$  grown on STO was obtained. The value of the refractive index at  $\lambda = 600$  nm for BCTZ50 was  $n = 2.311$ , instead of  $n = 2.332$  for BCTZ50/STO. The values of the GSO extinction coefficients were found to be higher for samples grown on STO: a value of  $k = 0.45$  for BCTZ50/GSO and  $k = 0.7$  for BCTZ50/STO, respectively. The calculated indirect band gap was found to be  $E_g = 3.58$  eV for BCTZ50/GSO. The discrepancy between the optical constants values for samples grown on different substrates is explained by the crystallinity features of the thin films, induced by the substrate during PLD deposition process. For  $\text{GdScO}_3$ , the lattice parameters are  $a = 5.52$  Å,  $b = 5.79$  Å and

$c = 8.03 \text{ \AA}$  (orthorhombic system) and the accommodation of BCTZ structure on the GSO substrate is different, as compared with cubic STO, leading to different optical properties.

The optical packing density of the BCTZ samples were calculated from experimental values of “ $n$ ” for BCTZ thin films (calculated from SE) and bulk values for the refractive index ( $n = 2.42$ ) for pure BaTiO<sub>3</sub> [51] by using [52]:

$$P = \left( \frac{(n_f^2 - 1)}{(n_f^2 + 1)} \right) \times \left( \frac{n_b^2 + 2}{n_b^2 - 1} \right) \quad (1)$$

and the porosity ratio:

$$P_{or} = 1 - \left( \frac{n_f^2 - 1}{n_b^2 - 1} \right) \quad (2)$$

The values are presented in Table 3.

**Table 3.** The packing density and porosity for samples of BCTZx deposited by PLD on monocrytalline substrate.

Probe	Laser Pulses	Refractive Index ( $\lambda = 600 \text{ nm}$ )	Packing Density	Porosity (%)
BCTZ50/GSO	8000	2.33	0.961	8.8
BCTZ 50/STO	8000	2.335	0.966	8.34
BCTZ 50/STO	36,000	2.332	0.963	8.62
BCTZ 50/GSO	36,000	2.311	0.956	10.62

The BCTZ50/STO samples exhibit the highest values for packing density and lower porosity values, in contrast with the BCTZ50 samples deposited on GSO substrate, for which a lower value for packing density (0.956) and a high porosity of 10.62% were calculated.

### 3.4. SAW Measurements

The SAW sensor testing system consisted of an amplifier and a frequency counter connected to a computer with specialised software (Figure 8). The gas flow was ensured by a mass flow controller through a mass flow meter.

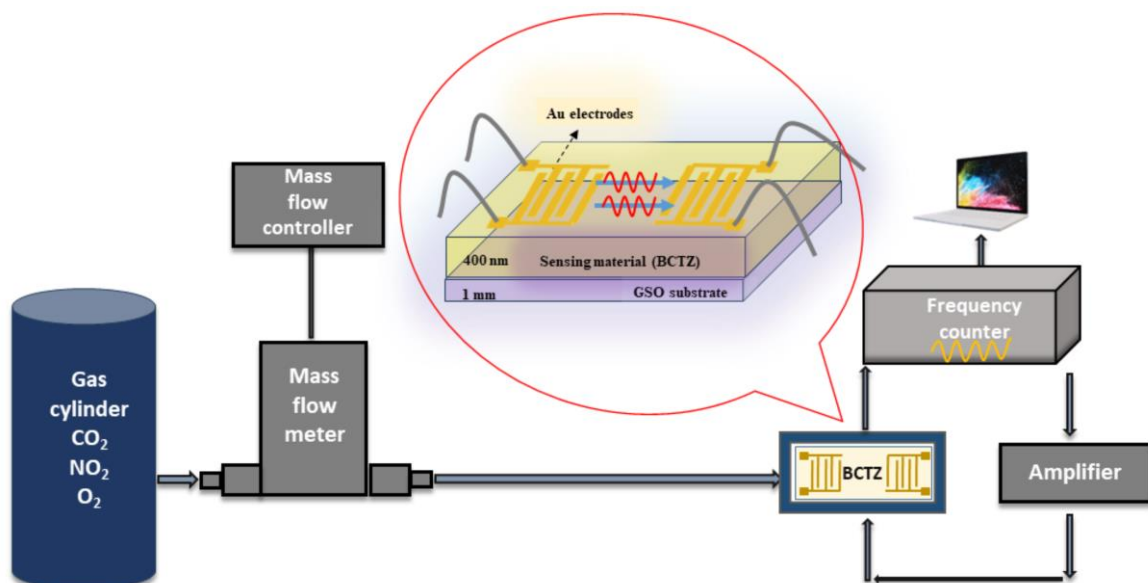


**Figure 8.** Experimental setup for SAW sensor frequency shift measurements.

The gases used for the tests were carbon dioxide (CO<sub>2</sub>), nitrogen (N<sub>2</sub>) and oxygen (O<sub>2</sub>), and the tests were carried out at a concentration of 99.996% N<sub>2</sub>, 99.999% O<sub>2</sub>, 99.998% CO<sub>2</sub> and a gas flow of 500 sccm.

The first important aspect noted from the frequency shifts was that the sensors with a PEI-sensitive layer had a higher frequency shift than those without a polymeric layer. At the same time, the sensors based on BCTZ50 deposited on an SrTiO<sub>3</sub> substrate had a small response or did not exhibit any response without the polymeric sensitive layer. A higher response was obtained for BCTZ50 deposited on a GdScO<sub>3</sub> substrate with a frequency shift between 12–19 KHz (Figure 9). In the case of BCTZ50/SrTiO<sub>3</sub>, when the thickness was increased by a higher number of laser pulses, the response of the SAW sensor became unclear and very noisy and we cannot accurately state the existence of a gas response (for example BCTZ50 deposited with 36,000 laser pulses in Figure 10). The test response from the PEI/BCTZ50/STO (8000 pulses), presented in Figure 11, sensor indicates a greater efficiency when testing for N<sub>2</sub>, with 12.66 kHz frequency shift, compared to responses of 9 kHz for O<sub>2</sub> and 11.29 kHz for CO<sub>2</sub>.

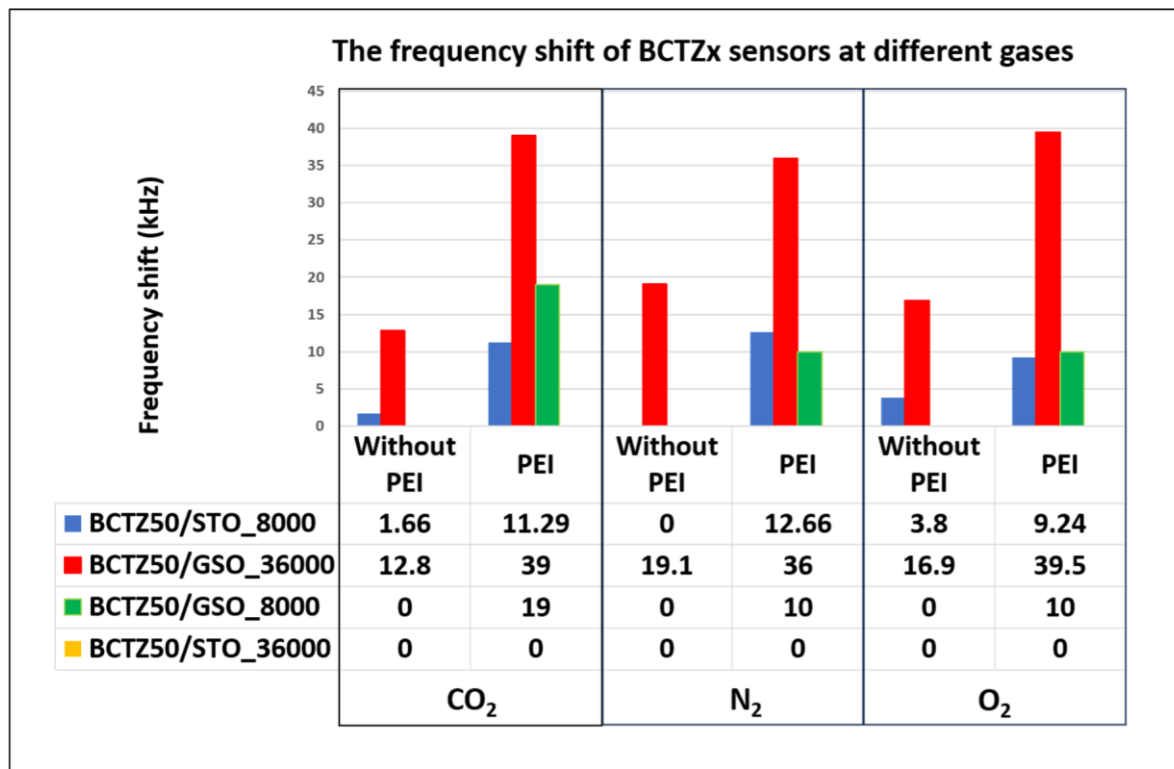


**Figure 9.** The frequency shift of BCTZx sensors at different gases.

The best results for the frequency shifts were obtained in the case of PEI/BCTZ50/GSO thin films. The highest frequency shift was about 39 kHz, obtained for O<sub>2</sub> and CO<sub>2</sub> gases by the PEI/BCTZ50/GSO-based SAW sensor. The values of the frequency shifts for these sensors were not contrasting, even when comparing different types of gases tested, which means that we cannot state if they are selective sensors.

The response time of the sensors was also influenced by the presence of the polymeric layer. Although we observed that, for BCTZ50/GSO sensors, the frequency shift was improved with the use of the polymeric coating, the influence on the response time was both increasing and decreasing. This increase in response time is explained by the fact that the adsorption of molecules at the level of the sensitive layer takes place more slowly than when gas molecules come into direct contact with the sensor substrate. However, considering that the frequency shift increases when using the polymer, an increase in the

response time is allowed. The BCTZ50/GSO sensor, in the tests for CO<sub>2</sub>, obtained both a decrease in the response time and an increase in the frequency shift (Figure 9).

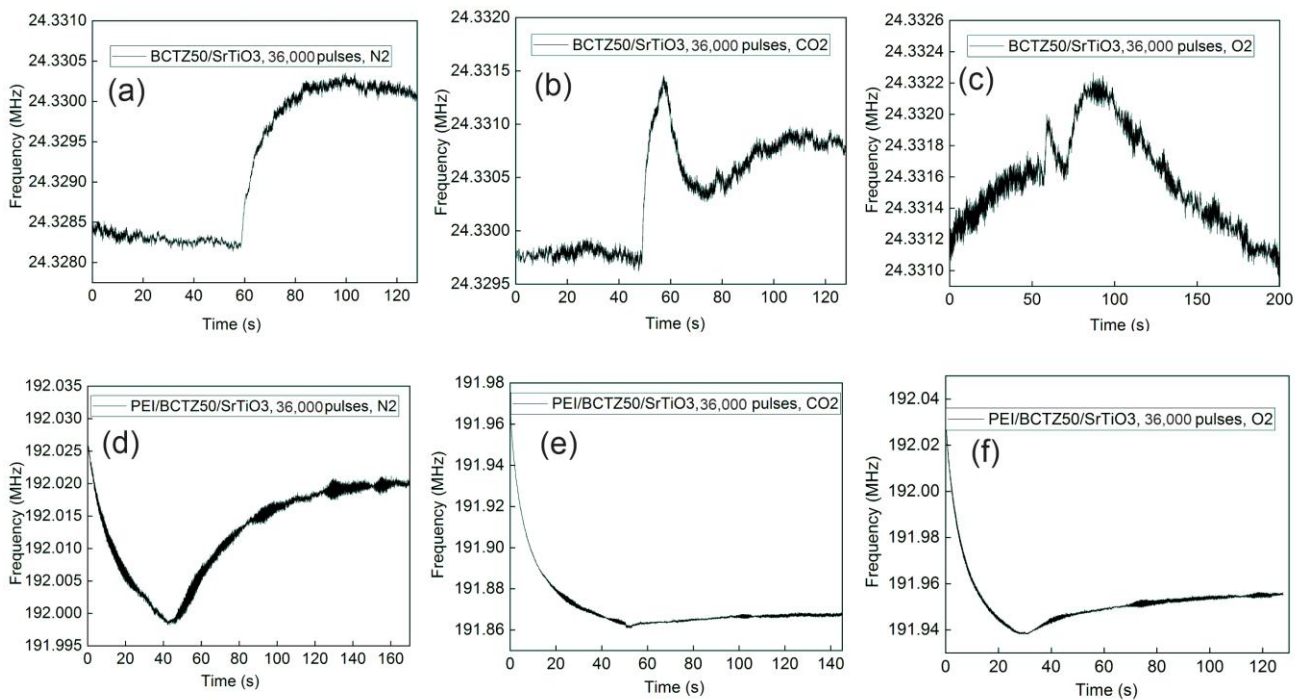


**Figure 10.** The gas response for the BCTZ50 deposited on SrTiO<sub>3</sub> substrate by PLD with 36,000 laser pulses without polymers for (a) N<sub>2</sub>; (b) CO<sub>2</sub>; (c) O<sub>2</sub>; and PEI/BCTZ50 for (d) N<sub>2</sub>; (e) CO<sub>2</sub>; (f) O<sub>2</sub>.

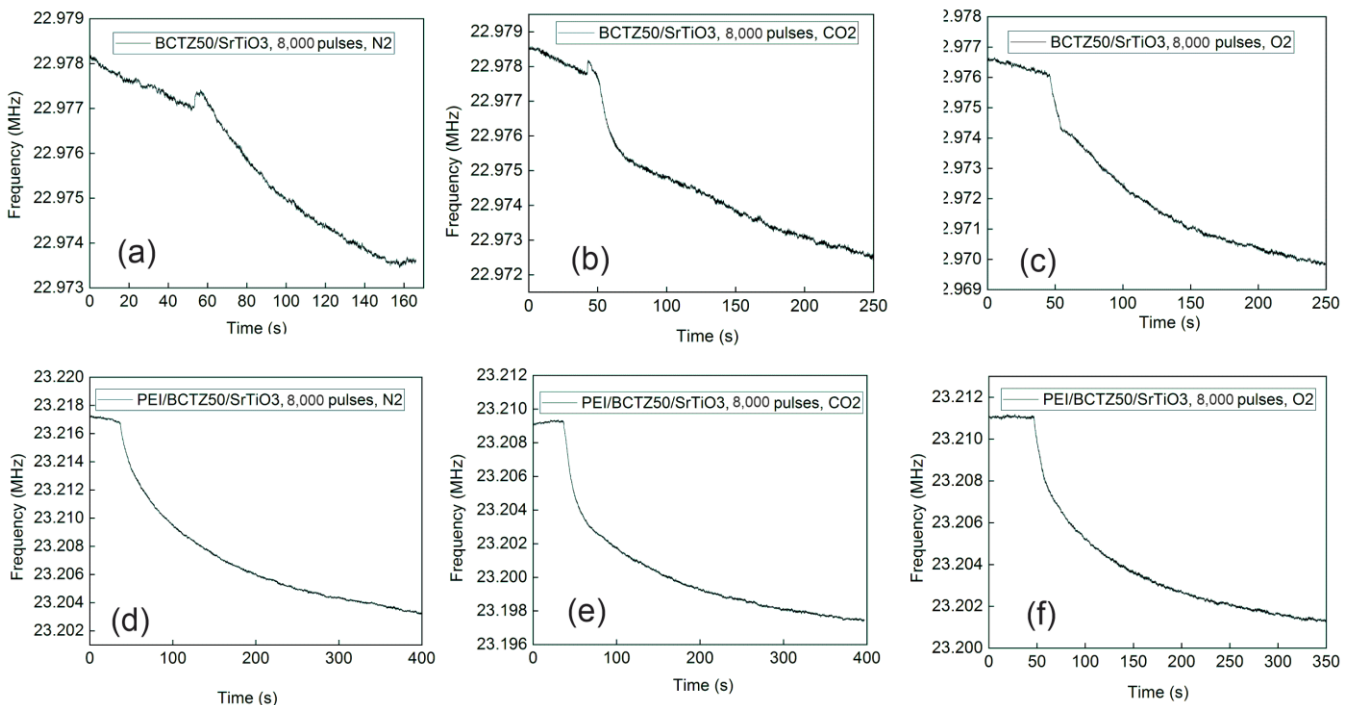


**Figure 11.** The gas response for the BCTZ50 deposited on SrTiO<sub>3</sub> substrate by PLD with 8000 laser pulses without polymers for (a) N<sub>2</sub>; (b) CO<sub>2</sub>; (c) O<sub>2</sub>; and BCTZ50 with PEI polymer for (d) N<sub>2</sub>; (e) CO<sub>2</sub>; (f) O<sub>2</sub>.

The mechanism of gas sensing was explained by Wang et al. [53]. When gas molecules interact with surface of an oxide, the charge state is altered, and the conductivity of sample

is changed. A change in the conductivity of layer leads to a change in SAW sensor response. For all samples deposited with 8000 laser pulses, we calculated, from optical analysis, a percentage of pores around 6–8%. From Figures 10 and 11, we can observe the response for BCTZ50/STO without a polymeric layer in the presence of two analysed gases ( $O_2$  and  $CO_2$ ). The presence of pores causes oxygen to be easily adsorbed and the high porosity provides a larger amount of surface sites for gas adsorption and chemical reactions [54]. This may attract more electrons from the BCTZ layer and substantially modify their frequency response in SAW measurement configuration. This behaviour in  $BaTiO_3$ -based materials was already reported by Park et al. [55] in the case of  $Sb_2O_3$ - $BaTiO_3$ , and they showed the importance of porosity for gas response in the case of  $Sb_2O_3$ - $BaTiO_3$ . Moreover, other studies reported similar response behaviours for CO sensing, such as in the case of  $SnO_2$ , which has higher sensitivities but a smaller grain size [56–58].

By adding a polymer layer (PEI in this case), the mechanism behind overall response was changed. This time, the gas molecules were absorbed by the PEI layer, and because BCTZ is a piezoelectric material, changing the mass of the polymeric cover layer induced a response in the BCTZ film. The frequency shifts in samples with a polymeric layer were around 9–11 KHz for  $CO_2$  and  $O_2$ , and this is normal behavior for PEI [59].

When the number of laser pulses increased to 36,000 and the thickness of BCTZ50/STO layer increased more than three times, a strange behaviour was observed in the gas response. For  $N_2$  in the case of the BCTZ50/STO with a thickness of ~300 nm the frequency response was noisy, but when  $N_2$  was introduced in testing chamber, a shift was observed (Figure 10). For  $CO_2$  and  $O_2$  the shift was noticeable but weak and the frequency response became noisy and unstable in a matter of a few seconds after the gas was introduced. Even with PEI layer, the gas response was not clear. At high thicknesses, the properties of the BCTZ thin layer were similar to bulk BCTZ, and because there was no gas response for thicker BCTZ50/STO, we can conclude that this material is only suitable for gas detection when the functional properties are altered by structural strain.

In the case of BCTZ50 thin films deposited on GSO, the gas response as a function of thickness/strain relaxation was completely different in respect to the BCTZ50/STO films. For the thin, 8000 laser-pulsed BCTZ50/GSO sample without the PEI coating, only a weak response in the presence of  $CO_2$  was noticed. For the BCTZ 50/GSO thin films, the frequency measured during time before and after gas was introduced to the chamber are presented in Figures 12 and 13. For the thickest BCTZ50/GSO sample, a good response was noted without the polymer layer for all analysed gases, with a frequency shift between 12 and 39 KHz. The best response time for the thick BCTZ50/GSO sample was around 80 s in the case of oxygen gas detection. By adding a polymer layer, the frequency shift was increased to ~50 KHz; a higher frequency shift translated into a better response for all gases, but for  $CO_2$ , the response time was also increased a few times. The highest response time can be explained by a slow chemical reaction between the polymer and the gas molecules.

The difference between the gas responses from BCTZ deposited on different substrates were clearly observable, and in close correlation with crystalline features of the samples. As the in-plane strain- $\epsilon$  (%) in the BCTZ50/GSO samples is much smaller than in the case of the BCTZ50/STO samples, combined with the improved mosaicity (FWHM- $\omega(002)$ ), it is clear that the less-structurally defective BCTZ50/GSO films are suitable for acoustic wave propagation within the films in contrast with the BCTZ50/STO ones.

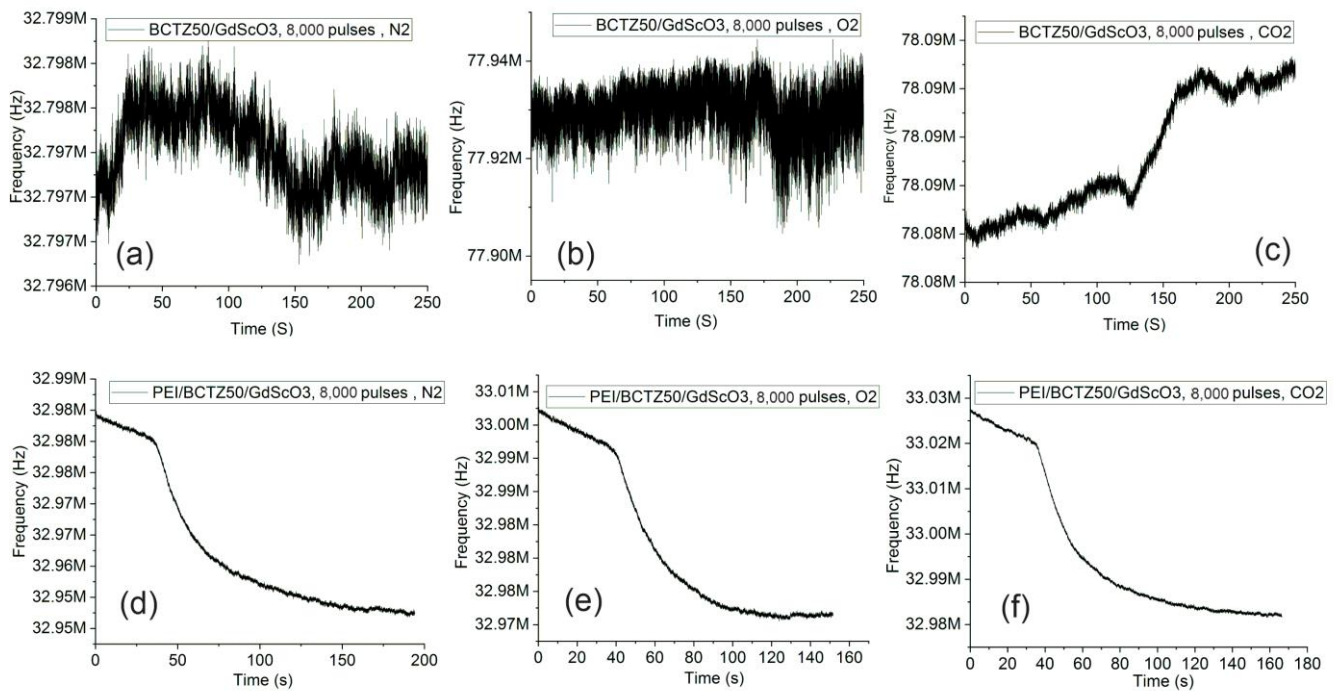


**Figure 12.** The gas response for the BCTZ50 deposited on GdScO<sub>3</sub> substrate by PLD with 8000 laser pulses without polymer for (a) N<sub>2</sub>; (b) CO<sub>2</sub>; (c) O<sub>2</sub>; and PEI/BCTZ50 for (d) N<sub>2</sub>; (e) CO<sub>2</sub>; (f) O<sub>2</sub>.

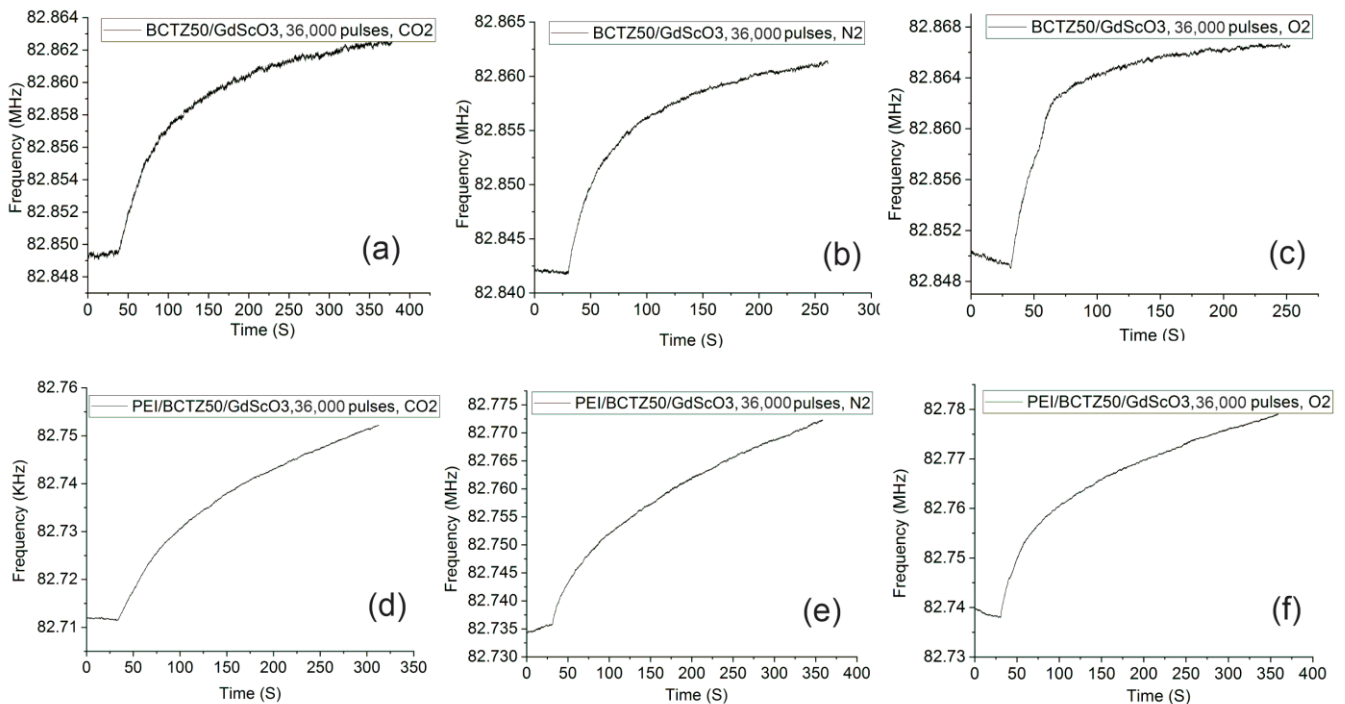


**Figure 13.** The gas response for the BCTZ50 deposited on GdScO<sub>3</sub> substrate by PLD with 36,000 laser pulses without polymer for (a) N<sub>2</sub>; (b) CO<sub>2</sub>; (c) O<sub>2</sub> and PEI/BCTZ50 for (d) N<sub>2</sub>; (e) CO<sub>2</sub>; (f) O<sub>2</sub>.

#### 4. Conclusions

Here, gas sensing performance as a function of thickness and substrate variation in BCTZ50 and PEI/BCTZ50 thin films deposited by laser-based techniques, in correlation with morphological, structural and optical characteristics, has been presented. BCTZ50 samples with different thicknesses were deposited on two types of substrates with different crystal structures, cubic (SrTiO<sub>3</sub>) and orthorhombic (GdScO<sub>3</sub>). Spectrometric ellipsometry

investigations revealed that, when the sample thickness increased, the thin film relaxed, and the optical properties were found to be similar with bulk BCTZ. The values of the GSO extinction coefficients were found to be higher for samples grown on STO, and the difference between optical constants values for samples grown on different substrates can be explained by the crystallinity of thin films, induced by the substrate during the PLD deposition process. After depositing IDT Au electrodes, the thin films were integrated into SAW devices in order to measure the frequency response to various gases (N<sub>2</sub>, CO<sub>2</sub> and O<sub>2</sub>). The response of BCTZ50 and PEI/BCTZ50 sensors was evaluated. The first important aspect noted from the frequency shifts was that the sensors with a PEI-sensitive layer had a higher frequency shift than those without a polymeric layer. At the same time, the sensors based on BCTZ50 and deposited with 8000 laser pulses on a SrTiO<sub>3</sub> substrate did not have such a high response without a polymeric sensitive layer. The test response of the BCTZ50/GSO sensor was 17.6 kHz with PEI and 19.1 kHz without PEI, indicating a greater efficiency when testing for N<sub>2</sub>. The best efficiency when testing for O<sub>2</sub> was recorded for PEI/BCTZ50, with a value of 39.5 kHz, more than two times higher compared to the film without the polymeric layer. The best results of the frequency shifts were obtained by the PEI/BCTZ50 sensors deposited on GdScO<sub>3</sub>; this was also the best when detecting CO<sub>2</sub>, with a recorded frequency shift of 39 kHz. In the case of CO<sub>2</sub> detection, when using PEI, the frequency shift increase was more than three times recorded for bare BCTZ50/GSO. The response time of the sensors was also influenced by the presence or absence of the polymeric layer, noting an increase in the response time when using PEI. This behaviour resulted from the fact that the adsorption of molecules at the level of the sensitive layer takes place more slowly than when gas molecules come into direct contact with the sensor substrate, thus an increase in the response time with an increase in the frequency shift is acceptable.

**Author Contributions:** Conceptualization, N.E., V.I., C.V. and N.D.S.; PLD and MAPLE experiments N.E. and M.L.S.; investigation, N.E., V.I., A.B., I.C., R.B. and C.V.; writing—original draft preparation, N.E. and V.I.; writing—review and editing, N.E., V.I. and N.D.S.; supervision, N.D.S.; funding acquisition, V.I. and N.D.S. All authors have read and agreed to the published version of the manuscript.

**Funding:** This work was supported by a grant of the Romanian Ministry of Education and Research, CCCDI-UEFISCDI, project number PN-III-P2-2.1-PED-2019-4734, within PNCDI III.

**Data Availability Statement:** The data presented in this study are available on request from the corresponding author.

**Acknowledgments:** The authors would like to acknowledge the contribution of Cristina Craciun for AFM investigations. SEM images were obtained using C400 PHOTOPLASMAT facilities acquired within the POC153/2016 IN2-FOTOPLASMAT project.

**Conflicts of Interest:** The authors declare no conflicts of interest.

## References

1. Wang, J.L.; Guo, Y.J.; Long, G.D.; Tang, Y.L.; Tang, Q.B.; Zu, X.T.; Ma, J.Y.; Du, B.; Torun, H.; Fu, Y.Q. Integrated sensing layer of bacterial cellulose and polyethyleneimine to achieve high sensitivity of ST-cut quartz surface acoustic wave formaldehyde gas sensor. *J. Hazard. Mater.* **2020**, *388*, 121743. [[CrossRef](#)] [[PubMed](#)]
2. Wang, W.; Liu, X.; Mei, S.; Jia, Y.; Liu, M.; Xue, X.; Yang, D. Development of a Pd/Cu nanowires coated SAW hydrogen gas sensor with fast response and recovery. *Sens. Actuators B Chem.* **2019**, *287*, 157–164. [[CrossRef](#)]
3. Rana, L.; Gupta, R.; Kshetrimayum, R.; Tomar, M.; Gupta, V. Fabrication of surface acoustic wave based wireless NO<sub>2</sub> gas sensor. *Surf. Coat. Technol.* **2018**, *343*, 89–92. [[CrossRef](#)]
4. Ghosh, A.; Zhang, C.; Shi, S.; Zhang, H. High temperature CO<sub>2</sub> sensing and its cross-sensitivity towards H<sub>2</sub> and CO gas using calcium doped ZnO thin film coated langasite SAW sensor. *Sens. Actuators B Chem.* **2019**, *301*, 126958. [[CrossRef](#)]
5. Tang, Y.; Li, D.; Ao, D.; Guo, Y.; Faheem, M.B.; Khan, B.; Zu, X.; Li, S. Highly sensitive surface acoustic wave HCl gas sensors based on hydroxyl-rich sol-gel AlOxOHy films. *Mater. Chem. Phys.* **2020**, *239*, 122026. [[CrossRef](#)]
6. Shu, L.; Jiang, T.; Xia, Y.; Wang, X.; Yan, D.; Wu, W. The Investigation of a SAW Oxygen Gas Sensor Operated at Room Temperature, Based on Nanostructured Zn<sub>x</sub>FeyO Films. *Sensors* **2019**, *19*, 3025. [[CrossRef](#)] [[PubMed](#)]

7. Constantinoiu, I.; Miu, D.; Viespe, C. Surface Acoustic Wave Sensors for Ammonia Detection at Room Temperature Based on SnO<sub>2</sub>/Co<sub>3</sub>O<sub>4</sub> Bilayers. *J. Sens.* **2019**, *2019*, 8203810. [[CrossRef](#)]
8. Yang, L.; Yin, C.; Zhang, Z.; Zhou, J.; Xu, H. The investigation of hydrogen gas sensing properties of SAW gas sensor based on palladium surface modified SnO<sub>2</sub> thin film. *Mater. Sci. Semicond. Process.* **2017**, *60*, 16–28. [[CrossRef](#)]
9. Tang, Y.; Xu, X.; Han, S.; Cai, C.; Du, H.; Zhu, H.; Zu, X.; Fu, Y. ZnO-Al<sub>2</sub>O<sub>3</sub> nanocomposite as a sensitive layer for high performance surface acoustic wave H<sub>2</sub>S gas sensor with enhanced elastic loading effect. *Sens. Actuators B Chem.* **2020**, *304*, 127395. [[CrossRef](#)]
10. Lim, J.-B.; Reddeppa, M.; Nam, D.; Pasupuleti, K.S.; Bak, N.-H.; Kim, S.-G.; Cho, H.D.; Kim, M.-D. Surface acoustic device for high response NO<sub>2</sub> gas sensor using p-phenylenediamine-reduced graphene oxide nanocomposite coated on langasite. *Smart Mater. Struct.* **2021**, *30*, 095016. [[CrossRef](#)]
11. Devkota, J.; Ohodnicki, P.; Greve, D. SAW Sensors for Chemical Vapors and Gases. *Sensors* **2017**, *17*, 801. [[CrossRef](#)] [[PubMed](#)]
12. Khlebarov, Z.P.; Stoyanova, A.I.; Topalova, D.I. Surface acoustic wave gas sensors. *Sens. Actuators B Chem.* **1992**, *8*, 33–40. [[CrossRef](#)]
13. Shen, C.-Y.; Huang, C.-P.; Huang, W.-T. Gas-detecting properties of surface acoustic wave ammonia sensors. *Sens. Actuators B Chem.* **2004**, *101*, 1–7. [[CrossRef](#)]
14. Caliendo, C.; Verardi, P.; Verona, E.; D’Amico, A.; Natale, C.D.; Saggio, G.; Serafini, M.; Paolesse, R.; Huq, S.E. Advances in SAW-based gas sensors. *Smart Mater. Struct.* **1997**, *6*, 689–699. [[CrossRef](#)]
15. Midhuna, A.S.; Shiju, B.S.; Sreenidhi, P.R. Optimizing Design of Surface Acoustic Wave Gas Sensor. In Proceedings of the 2021 5th International Conference on Trends in Electronics and Informatics (ICOEI), Tirunelveli, India, 3–5 June 2021; pp. 143–148. [[CrossRef](#)]
16. Liu, B.; Chen, X.; Cai, H.; Mohammad Ali, M.; Tian, X.; Tao, L.; Yang, Y.; Ren, T. Surface acoustic wave devices for sensor applications. *J. Semicond.* **2016**, *37*, 021001. [[CrossRef](#)]
17. Jakubik, W.P. Surface acoustic wave-based gas sensors. *Thin Solid Films* **2011**, *520*, 986–993. [[CrossRef](#)]
18. Hamidon, M.N.; Yunusa, Z. Sensing Materials for Surface Acoustic Wave Chemical Sensors. In *Progresses in Chemical Sensor*; Wang, W., Ed.; InTech: Vienna, Austria, 2016. [[CrossRef](#)]
19. Liu, X.; Cheng, S.; Liu, H.; Hu, S.; Zhang, D.; Ning, H. A Survey on Gas Sensing Technology. *Sensors* **2012**, *12*, 9635–9665. [[CrossRef](#)] [[PubMed](#)]
20. Luo, W.; Fu, Q.; Zhou, D.; Deng, J.; Liu, H.; Yan, G. A surface acoustic wave H<sub>2</sub>S gas sensor employing nanocrystalline SnO<sub>2</sub> thin film. *Sens. Actuators B Chem.* **2013**, *176*, 746–752. [[CrossRef](#)]
21. Dickert, F.L.; Forth, P.; Bulst, W.-E.; Fischerauer, G.; Knauer, U. SAW devices-sensitivity enhancement in going from 80 MHz to 1 GHz. *Sens. Actuators B Chem.* **1998**, *46*, 120–125. [[CrossRef](#)]
22. Sayago, I.; Fernandez, M.J.; Fontecha, J.L.; Horrillo, M.C.; Terrado, E.; Seral-Ascaso, A.; Munoz, E. Carbon nanotube-based SAW sensors. In Proceedings of the 2013 Spanish Conference on Electron Devices, Valladolid, Spain, 12–14 February 2013; IEEE: Valladolid, Spain, 2013; pp. 127–130. [[CrossRef](#)]
23. Sayago, I.; Fernández, M.J.; Fontecha, J.L.; Horrillo, M.C.; Vera, C.; Obieta, I.; Bustero, I. New sensitive layers for surface acoustic wave gas sensors based on polymer and carbon nanotube composites. *Sens. Actuators B Chem.* **2012**, *175*, 67–72. [[CrossRef](#)]
24. Asad, M.; Sheikhi, M.H. Surface acoustic wave based H<sub>2</sub>S gas sensors incorporating sensitive layers of single wall carbon nanotubes decorated with Cu nanoparticles. *Sens. Actuators B Chem.* **2014**, *198*, 134–141. [[CrossRef](#)]
25. Xu, S.; Li, C.; Li, H.; Li, M.; Qu, C.; Yang, B. Carbon dioxide sensors based on a surface acoustic wave device with a graphene-nickel-L-alanine multilayer film. *J. Mater. Chem. C* **2015**, *3*, 3882–3890. [[CrossRef](#)]
26. Wang, S.-H.; Shen, C.-Y.; Su, J.-M.; Chang, S.-W. A Room Temperature Nitric Oxide Gas Sensor Based on a Copper-Ion-Doped Polyaniline/Tungsten Oxide Nanocomposite. *Sensors* **2015**, *15*, 7084–7095. [[CrossRef](#)] [[PubMed](#)]
27. Sadek, A.Z.; Wlodarski, W.; Shin, K.; Kaner, R.B.; Kalantar-zadeh, K. A layered surface acoustic wave gas sensor based on a polyaniline/In<sub>2</sub>O<sub>3</sub> nanofibre composite. *Nanotechnology* **2006**, *17*, 4488–4492. [[CrossRef](#)]
28. Sil, D.; Hines, J.; Udeoyo, U.; Borguet, E. Palladium Nanoparticle-Based Surface Acoustic Wave Hydrogen Sensor. *ACS Appl. Mater. Interfaces* **2015**, *7*, 5709–5714. [[CrossRef](#)]
29. Robinson, A.L.; Stavila, V.; Zeitler, T.R.; White, M.I.; Thornberg, S.M.; Greathouse, J.A.; Allendorf, M.D. Ultrasensitive Humidity Detection Using Metal–Organic Framework-Coated Microsensors. *Anal. Chem.* **2012**, *84*, 7043–7051. [[CrossRef](#)] [[PubMed](#)]
30. Tasaltin, C.; Ebeoglu, M.A.; Ozturk, Z.Z. Acoustoelectric Effect on the Responses of SAW Sensors Coated with Electrospun ZnO Nanostructured Thin Film. *Sensors* **2012**, *12*, 12006–12015. [[CrossRef](#)]
31. Kumar, A.; Prajesh, R. The potential of acoustic wave devices for gas sensing applications. *Sens. Actuators Phys.* **2022**, *339*, 113498. [[CrossRef](#)]
32. Omori, T.; Hashimoto, K.; Yamaguchi, M. PZT Thin Films for SAW and BAW Devices, Engineering, Materials Science, Physics, Department of Electronics and Mechanical Engineering, Chiba University Inage-ku, Chiba-shi, 263-8522, Japan. Available online: <https://www.te.chiba-u.jp/lab/ken/Symp/Symp2001/PAPER/OMORI.PDF> (accessed on 27 October 2022).
33. Hsiao, Y.-J.; Fang, T.-H.; Chang, Y.-H.; Chang, Y.-S.; Wu, S. Surface acoustic wave characteristics and electromechanical coupling coefficient of lead zirconate titanate thin films. *Mater. Lett.* **2006**, *60*, 1140–1143. [[CrossRef](#)]
34. Shilpa, G.D.; Sreelakshmi, K.; Ananthaprasad, M.G. PZT thin film deposition techniques, properties and its application in ultrasonic MEMS sensors: A review. *IOP Conf. Ser. Mater. Sci. Eng.* **2016**, *149*, 012190. [[CrossRef](#)]

35. Takenaka, T. Lead-free piezo-ceramics. In *Advanced Piezoelectric Materials*; Elsevier: Amsterdam, The Netherlands, 2010; pp. 130–170. [[CrossRef](#)]
36. Jaffe, W.R.C.B.; Jaffe, H. *Piezoelectric Ceramics*, 1st ed.; Academic Press: Cambridge, MA, USA, 1971.
37. Liu, W.; Ren, X. Large Piezoelectric Effect in Pb-Free Ceramics. *Phys. Rev. Lett.* **2009**, *103*, 257602. [[CrossRef](#)] [[PubMed](#)]
38. Gao, J.; Xue, D.; Liu, W.; Zhou, C.; Ren, X. Recent Progress on BaTiO<sub>3</sub>-Based Piezoelectric Ceramics for Actuator Applications. *Actuators* **2017**, *6*, 24. [[CrossRef](#)]
39. Li, W.L.; Zhang, T.D.; Xu, D.; Hou, Y.F.; Cao, W.P.; Fei, W.D. LaNiO<sub>3</sub> seed layer induced enhancement of piezoelectric properties in (100)-oriented (1-x)BZT-xBCT thin films. *J. Eur. Ceram. Soc.* **2015**, *35*, 2041–2049. [[CrossRef](#)]
40. Li, W.L.; Zhang, T.D.; Hou, Y.F.; Zhao, Y.; Xu, D.; Cao, W.P.; Fei, W.D. Giant piezoelectric properties of BZT-0.5BCT thin films induced by nanodomain structure. *RSC Adv.* **2014**, *4*, 56933–56937. [[CrossRef](#)]
41. Scarisoreanu, N.D.; Craciun, F.; Moldovan, A.; Ion, V.; Birjega, R.; Ghica, C.; Negrea, R.F.; Dinescu, M. High Permittivity (1-x)Ba(Zr<sub>0.2</sub>Ti<sub>0.8</sub>)O<sub>3</sub>-x(Ba<sub>0.7</sub>Ca<sub>0.3</sub>)TiO<sub>3</sub> (x = 0.45) Epitaxial Thin Films with Nanoscale Phase Fluctuations. *ACS Appl. Mater. Interfaces* **2015**, *7*, 23984–23992. [[CrossRef](#)] [[PubMed](#)]
42. Yan, Y.; Yang, G.; Xu, J.-L.; Zhang, M.; Kuo, C.-C.; Wang, S.-D. Conducting polymer-inorganic nanocomposite-based gas sensors: A review. *Sci. Technol. Adv. Mater.* **2020**, *21*, 768–786. [[CrossRef](#)] [[PubMed](#)]
43. Fratoddi, I.; Venditti, I.; Cametti, C.; Russo, M.V. Chemiresistive polyaniline-based gas sensors: A mini review. *Sens. Actuators B Chem.* **2015**, *220*, 534–548. [[CrossRef](#)]
44. Bartlett, P.N.; Archer, P.B.M.; Ling-Chung, S.K. Conducting polymer gas sensors part I: Fabrication and characterization. *Sens. Actuators* **1989**, *19*, 125–140. [[CrossRef](#)]
45. Dinca, V.; Viespe, C.; Brajnicov, S.; Constantinoiu, I.; Moldovan, A.; Bonciu, A.; Toader, C.; Ginghina, R.; Grigoriu, N.; Dinescu, M.; et al. MAPLE Assembled Acetylcholinesterase–Polyethylenimine Hybrid and Multilayered Interfaces for Toxic Gases Detection. *Sensors* **2018**, *18*, 4265. [[CrossRef](#)]
46. Regensburger, S.; Mohammadi, M.; Khawaja, A.A.; Radetinac, A.; Komissinskiy, P.; Alff, L.; Preu, S. Optical Properties of Highly Conductive SrMoO<sub>3</sub> Oxide Thin Films in the THz Band and Beyond. *J. Infrared Millim. Terahertz Waves* **2020**, *41*, 1170–1180. [[CrossRef](#)]
47. Scarisoreanu, N.D.; Craciun, F.; Birjega, R.; Ion, V.; Teodorescu, V.S.; Ghica, C.; Negrea, R.; Dinescu, M. Joining Chemical Pressure and Epitaxial Strain to Yield Y-doped BiFeO<sub>3</sub> Thin Films with High Dielectric Response. *Sci. Rep.* **2016**, *6*, 25535. [[CrossRef](#)] [[PubMed](#)]
48. Metzger, T.; Höppler, R.; Born, E.; Ambacher, O.; Stutzmann, M.; Stömmer, R.; Schuster, M.; Göbel, H.; Christiansen, S.; Albrecht, M.; et al. Defect structure of epitaxial GaN films determined by transmission electron microscopy and triple-axis X-ray diffractometry. *Philos. Mag. A* **1998**, *77*, 1013–1025. [[CrossRef](#)]
49. Schwarzkopf, J.; Braun, D.; Schmidbauer, M.; Duk, A.; Wördenweber, R. Ferroelectric domain structure of anisotropically strained NaNbO<sub>3</sub> epitaxial thin films. *J. Appl. Phys.* **2014**, *115*, 204105. [[CrossRef](#)]
50. Spectroscopic Ellipsometry: Principles and Applications | Wiley. Available online: <https://www.wiley.com/en-us/Spectroscopic+Ellipsometry:+Principles+and+Applications-p-9780470016084> (accessed on 27 October 2022).
51. Liu, D.; Shim, J.; Sun, Y.; Li, Q.; Yan, Q. Growth of Ca, Zr co-doped BaTiO<sub>3</sub> lead-free ferroelectric single crystal and its room-temperature piezoelectricity. *AIP Adv.* **2017**, *7*, 095311. [[CrossRef](#)]
52. Wemple, S.H.; Didomenico, M.; Camlibel, I. Dielectric and optical properties of melt-grown BaTiO<sub>3</sub>. *J. Phys. Chem. Solids* **1968**, *29*, 1797–1803. [[CrossRef](#)]
53. Santhosh Kumar, T.; Bhuyan, R.K.; Pamu, D. Effect of post annealing on structural, optical and dielectric properties of MgTiO<sub>3</sub> thin films deposited by RF magnetron sputtering. *Appl. Surf. Sci.* **2013**, *264*, 184–190. [[CrossRef](#)]
54. Wang, C.; Yin, L.; Zhang, L.; Xiang, D.; Gao, R. Metal Oxide Gas Sensors: Sensitivity and Influencing Factors. *Sensors* **2010**, *10*, 2088–2106. [[CrossRef](#)]
55. Park, K.; Seo, D.J. Gas sensing characteristics of BaTiO<sub>3</sub>-based ceramics. *Mater. Chem. Phys.* **2004**, *85*, 47–51. [[CrossRef](#)]
56. Li, F.; Xu, J.; Yu, X.; Chen, L.; Zhu, J.; Yang, Z.; Xin, X. One-step solid-state reaction synthesis and gas sensing property of tin oxide nanoparticles. *Sens. Actuators B Chem.* **2002**, *81*, 165–169. [[CrossRef](#)]
57. Yamazoe, N. New approaches for improving semiconductor gas sensors. *Sens. Actuators B Chem.* **1991**, *5*, 7–19. [[CrossRef](#)]
58. Van Toan, N.; Viet Chien, N.; Van Duy, N.; Si Hong, H.; Nguyen, H.; Duc Hoa, N.; Van Hieu, N. Fabrication of highly sensitive and selective H<sub>2</sub> gas sensor based on SnO<sub>2</sub> thin film sensitized with micro-sized Pd islands. *J. Hazard. Mater.* **2016**, *301*, 433–442. [[CrossRef](#)]
59. Sun, B.; Xie, G.; Jiang, Y.; Li, X. Comparative CO<sub>2</sub>-Sensing Characteristic Studies of PEI and PEI/Starch Thin Film Sensors. *Energy Procedia* **2011**, *12*, 726–732. [[CrossRef](#)]

**Disclaimer/Publisher’s Note:** The statements, opinions and data contained in all publications are solely those of the individual author(s) and contributor(s) and not of MDPI and/or the editor(s). MDPI and/or the editor(s) disclaim responsibility for any injury to people or property resulting from any ideas, methods, instructions or products referred to in the content.